npj | flexible electronics

Article

Published in partnership with Nanjing Tech University

https://doi.org/10.1038/s41528-026-00563-3

A bio-inspired origami capacitive robotic e-skin with multimodal sensing capabilities

Qian Xu[1], Boyang Zhang[1], Yik Kin Cheung[1], Zhiwei Yang[2], Rui Jiao[1], Shuhuai Yao[1], Wei Hong[2] ✉ & Hongyu Yu[3] ✉

As embodied intelligence emerges, flexible electronics are attracting attention in wearable technology, healthcare, robotics, and human-machine interfaces. Electronic skins (e-skins) are vital for safe, efficient interaction, yet the structural and wiring complexity of conventional sensor arrays hinders scalability. Inspired by fish skin, we propose an origami-with-scale-based capacitive electronic skin that covers a large area (60000 mm^2) and enables super-resolution tactile sensing by harnessing origami's deformation transmission. Interdigital electrodes provide shear-force sensing, while a proximity-sensing layer detects approaching conductive objects, providing collision protection for humans. Additionally, machine learning algorithms are employed to enhance sensing accuracy, achieving a super-resolution (SR) factor of 241 with average localization and force magnitude estimation error of less than 3.5 mm and 0.04 N, respectively. By integrating theoretical models and machine learning algorithms, multi-point touch for non-adjacent loads was also realized. This design delivers a compact, multifunctional solution for large-area, super-resolution tactile sensing, advancing safe, immersive human-machine interaction and embodied intelligence.

Flexible and stretchable electronic devices, especially tactile sensors and skins, have attracted significant interest for applications in wearable technology, healthcare, and robotics. Their mechanical flexibility and ability to conform to irregular surfaces make them ideal for soft, adaptive, and human-interactive systems. They are also durable and maintain stable performance under deformation. The shift from rigid substrates, such as silicon and PCBs, to flexible platforms has opened new possibilities in biomedical systems, wearable devices, and soft robotics.

There are numerous methods for the realization of tactile sensing; for example, piezoresistive[1–5], capacitive[6–9], piezoelectric[10,11], triboelectric[12,13], optical[14,15], magnetic[16–18], resonant[19,20], and field-effect transistor (FET)[21,22] based sensing mechanisms. These sensing mechanisms have allowed tactile devices to detect load magnitude, location, and direction[23–25]. Large-area coverage often requires dense sensor arrays. This high density leads to structural complexity, fabrication difficulties, wiring challenges, and increased costs.

To overcome these limitations, super-resolution (SR) tactile sensing has emerged[26], where the effective resolution exceeds the physical density of sensing units, analogous to biological hyperacuity (Note S1 and Fig. S1). The development of super-resolution theory and practice improves the spatial accuracy of tactile sensors and reduces wiring costs. This is achieved using structural innovations[24], field-based techniques, or machine learning[27,28].

Despite rapid advances, most recently developed tactile sensors remain limited in active area. Their super-resolution factors are usually below 100 (Table 1). This limitation hinders their use as large-area robotic skins. One main reason is that most tactile sensors are silicone-based. In silicone, deformation propagates only over a very restricted range (Fig. S7). Table 1 compares tactile sensor performance over the past few years. Only a small fraction of sensors achieve super-resolution factors in the hundreds. In conventional sensor arrays, super-resolution coefficients are typically small. Thus, large-area tactile sensing often requires many sensing units. This greatly increases wiring complexity and structural intricacy.

The origami structure offers a solution. As a paper-folding technique, it transforms 2D patterns into 3D structures. Most research on origami focuses on its stretchability[29,30], primarily concerning in-plane mechanical properties. Few studies examine out-of-plane properties. Origami transmits deformation and enables super-resolution tactile sensing in these directions, as shown in Note S2 and Figs. S2 and S3. This property allows for global deformation through local folding and unfolding, making origami suitable for large-area, super-resolution tactile sensing.

[1]Department of Mechanical and Aerospace Engineering, The Hong Kong University of Science and Technology, Hong Kong, China. [2]Department of Mechanics and Aerospace Engineering, Southern University of Science and Technology, Shenzhen, China. [3]Department of Mechanical Engineering, The Hong Kong Polytechnic University, Hong Kong, China. ✉e-mail: hongw@sustech.edu.cn; hongyu.yu@polyu.edu.hk

Table 1 | Comparisons of state-of-the-art tactile skins and our proposed origami capacitive e-skin

Sensor name	Transduction method	Area (mm^2)	SR factor	Thickness (*mm*)	Output (Position, Force)	Force estimation error (*N*)	Response time (*ms*)	Shear sensing	Fabrication complexity
Hu et.al.[35]	Magnetic	48400	669	~ 12	P, F	N.M.	~ 20	N.A.	High (special magnetization)
Leong et.al.[36]	Optical	144	127	~ 2	P, F	0.07	N.M.	N.A.	Low
Lu et.al.[37]	Resistive	520	5.9	~ 6	P, F	0.61	N.M.	N.A.	Low
Pereira et.al.[38]	Optical	9600	~ 30	~ 10	P	N.A.	N.M.	N.A.	Medium
Sohn et.al.[39]	Resistive	1600	~ 52	~ 5	P	N.A.	N.M.	N.A.	Low
Chen et.al.[40]	Resistive	40000	~ 35	2.95	P, F	0.6	170	N.A.	Medium
Shao et.al.[41]	Triboelectric	62500	~ 1	~ 2	P	N.A.	100	N.A.	Medium
Sun et.al.[26]	Barometer	676	40	10	P, F	0.01	N.M.	N.A.	Medium
Berman et.al.[42]	Capacitive	1225	~ 1	~ 1	P	N.A.	N.M.	N.A.	Low
Our work	Capacitive	60000 (demo)	241	9	P, F	0.06	~ 10	Yes	Medium

SR factor = Area/(tr×n×$RMSE_X$×$RMSE_Y$); RMSE root mean square error. For our capacitive e-skin, the SR factor can be increased to 542 when using only four electrodes. For sensors that do not specify RMSE, the mean error is used when calculating the SR factor.
N.M. Not mentioned, *N.A.* Not applicable.

Here, we propose a bio-inspired, origami-enabled, large-area capacitive e-skin. The origami structure serves as the skeleton and acts as both a deformation distributor and a directional transducer. It converts concentrated out-of-plane loads into a widespread in-plane deformation field (Fig. S2). This field can be detected by measuring capacitance changes across electrodes at different positions, thereby enabling the determination of both the location and magnitude of external loads. Furthermore, by implementing machine learning algorithms, the accuracy of single-point touch sensing has reached a high level, with an average localization error of less than 3.5 mm and an average force estimation error of less than 0.04 N. Simultaneously, through the integration of theoretical analysis and machine learning algorithms, multi-touch capability for non-adjacent loads has been realized. Furthermore, the electronic skin was installed on a robotic arm, demonstrating its potential for human-machine interaction.

Results

E-skin structure and sensing mechanism

Inspired by the structure of fish skin, the proposed e-skin comprises five layers, as shown in Fig. 1a: a proximity-sensing layer (aluminized PI film, 0.1 mm); elastomer scales (filling the concave areas on the upper surface of the origami structure, which share the same thickness as the origami structure without increasing the overall thickness); an origami-shaped flexible printed circuit (FPC) with double stiffeners (~ 4 mm when folded); a pillar array featuring a grounding electrode (4 mm); and a shear-sensing layer equipped with interdigital electrodes (1 mm), resulting in a total thickness of approximately 9 mm. The sensing mechanism is illustrated in Fig. 1b. Under normal load, the origami structure expands, thereby increasing the capacitance between the electrodes and the ground. Due to its deformation transmission capability, both the magnitude and location of normal loads can be determined by measuring capacitance changes across different electrodes. When a shear force is applied, the origami structure translates globally, and the shear-sensing layer deforms laterally, increasing the capacitance of the embedded interdigital electrodes. Additionally, when an external conductive object (e.g., a human hand) approaches, the capacitance between the object (ground) and the proximity-sensing layer (positive electrode) increases, enabling proximity sensing.

The origami skeleton design is based on the Miura-ori pattern[31]. Each unit cell has four congruent panels arranged periodically (Fig. 2a). A reduced panel dimension is preferred to decrease overall thickness and enhance usability. Considering application requirements and manufacturing constraints, the panel dimensions were fixed at $a = b = 10$ mm. To avoid directional dependence in out-of-plane deformation, identical Poisson's ratios were ensured by setting $\alpha = 50°$ and $\phi = 45°$ (Note S3, Figs. S4 and S5).

Ideal origami structures exhibit rigid-foldability[32]. However, soft face panels and finite crease thickness constrain deformation propagation. To address this, we designed an origami structure with double-layer stiffeners and crease optimizations (Fig. 2b). We narrowed the mountain folds and released the valley folds for the upper stiffeners, and reversed this for the lower ones. Foldability was significantly improved. Numerical simulations (Note S4 and Fig. S6) confirm that deformation propagation approaches the rigid-foldable state.

Although double layer stiffeners improve foldability, stress still concentrates at the vertices during folding due to geometric singularities. To mitigate this, vertex cuts were introduced at the vertices. Finite element analysis (FEA) results (Figs. 2c and S8) show that vertex cuts can effectively eliminate stress concentrations.

To support the origami structure and restore it to its initial state after unloading, a pillar array was designed and connected to the bottom vertices of the origami structure (Fig. 2d). Each pillar consists of three sections that form a circular groove for easy assembly. The pillar array also serves as grounding electrodes by incorporating a conductive tape layer. Pillar height affects capacitance. Simulations (Fig. 2e) of various pillar heights confirm that capacitance remains within the operation range of AD7147 (± 8 pF). To balance sensitivity and connectivity, $H_{p1} = 3$ mm, $H_{p2} = 2$ mm, and $H_{p3} = 0.5$ mm were chosen. To compensate for stiffness inhomogeneity between

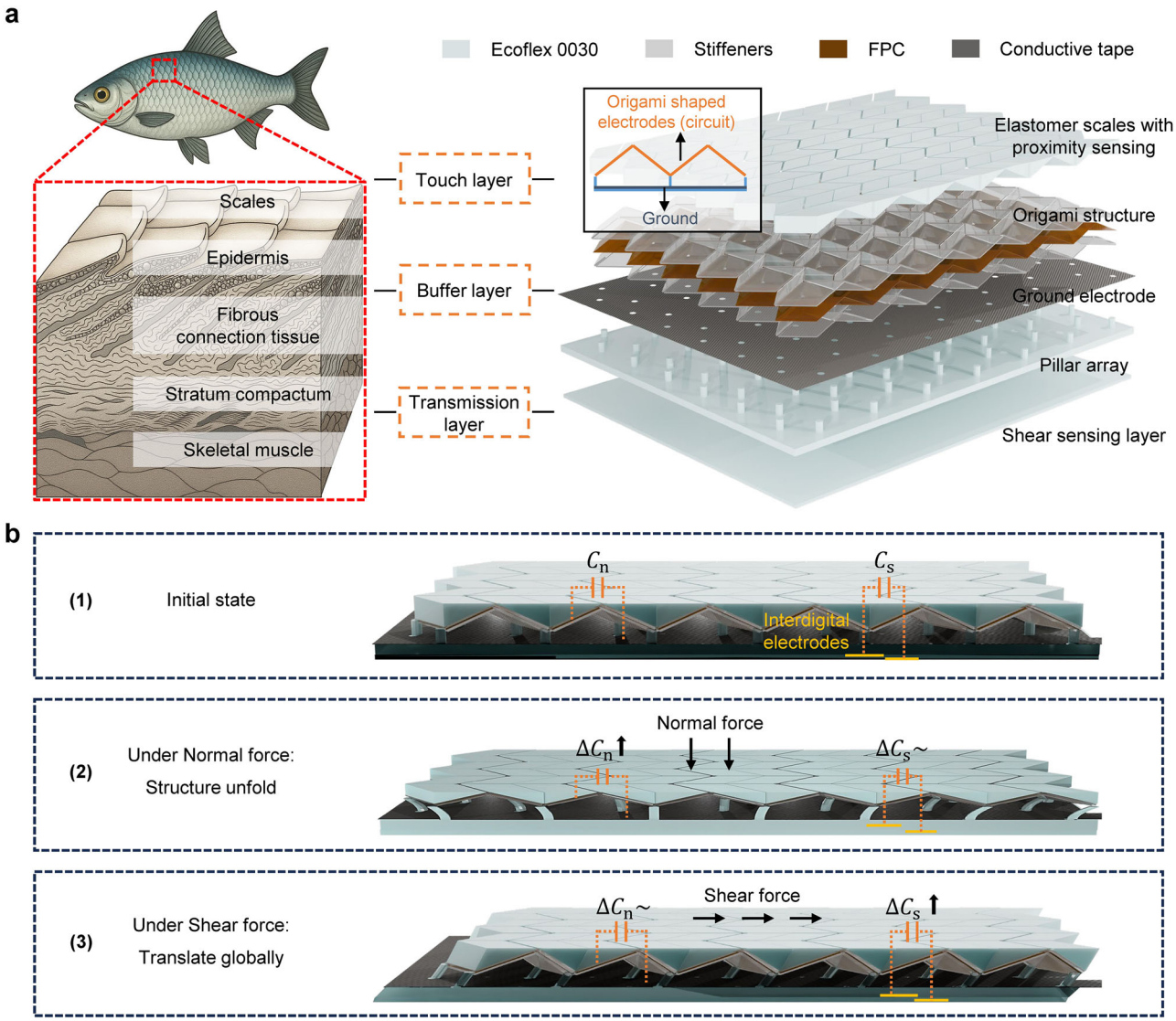

Fig. 1 | Structure and sensing mechanism of the proposed origami super-resolution e-skin. a Structure of the proposed e-skin. The small diagram shows the origami-shaped circuit with electrodes and ground. **b** Sensing mechanism. (1) Initial state. (2) Subject to a normal load, the structure unfolds, and the capacitance between origami panels and ground will increase, while the capacitance in the shear-sensing layer will remain almost constant. (3) Subject to a shear load, the origami structure translates due to the constraint from the elastomer scales, leading to a constant capacitance of origami panel capacitors and a significant capacitance variation in the shear-sensing layer.

central and edge cells, edge pillars were given larger radii. Specifically, D_{p1} = 2 mm for central pillars and 3 mm for edge pillars; D_{p2} is 1 mm and 2 mm for the central and edge pillars, respectively; D_{p3} equals D_{p1} to maintain stable connectivity.

Additionally, to enable shear-force sensing, a shear-sensing layer was introduced below the pillar array (Fig. 2f) that incorporated interdigital electrodes. Tests with varying electrode gaps (W) (Fig. 2g) show that smaller W increases shear-sensing sensitivity but reduces robustness against normal-load interference. A balanced design was achieved with an electrode width (W_e) of 5 mm and a gap (W) of 0.5 mm. Results (Fig. 2g) confirm negligible normal-load interference on shear sensing. Analysis of the electric potential and electric field distribution for the finalized design is presented in and Fig. S9.

Inspired by the structure of fish skin, elastomer scales were placed above the origami structure. These provide a flat contact surface, prevent unwanted folding under shear, to decouple shear from normal load measurements. The proximity-sensing layer, consisting of a single-sided aluminized polyimide (PI) film, was then added above the scales. This layer detects approaching conductive objects, such as humans, and prevents collisions.

Finally, since robotic surfaces are often curved rather than planar, a new skin geometry was designed to accommodate curvature via elastic energy minimization[33]. The resulting curved origami skin maintains the same multilayer structure. Further details are provided in Note S5 and Fig. S11.

Circuit design

The AD7147 capacitance-to-digital converter (CDC) was selected for capacitance measurement due to its multiple input channels, on-chip digitization, and convenient two-wire I2C interface. These features make it well-suited for large-area capacitive sensors with lower wiring complexity. Register read and write operations must be performed on the chip before use, as detailed in Note S6. The circuit schematic is shown in Fig. 3a. 'CIN' represents 13 inputs. The AD7147 communicates with the MCU (Arduino Uno) via I2C. For systems with multiple AD7147 devices, the TCA9548 I2C switch can be used for demultiplexing (Fig. S21).

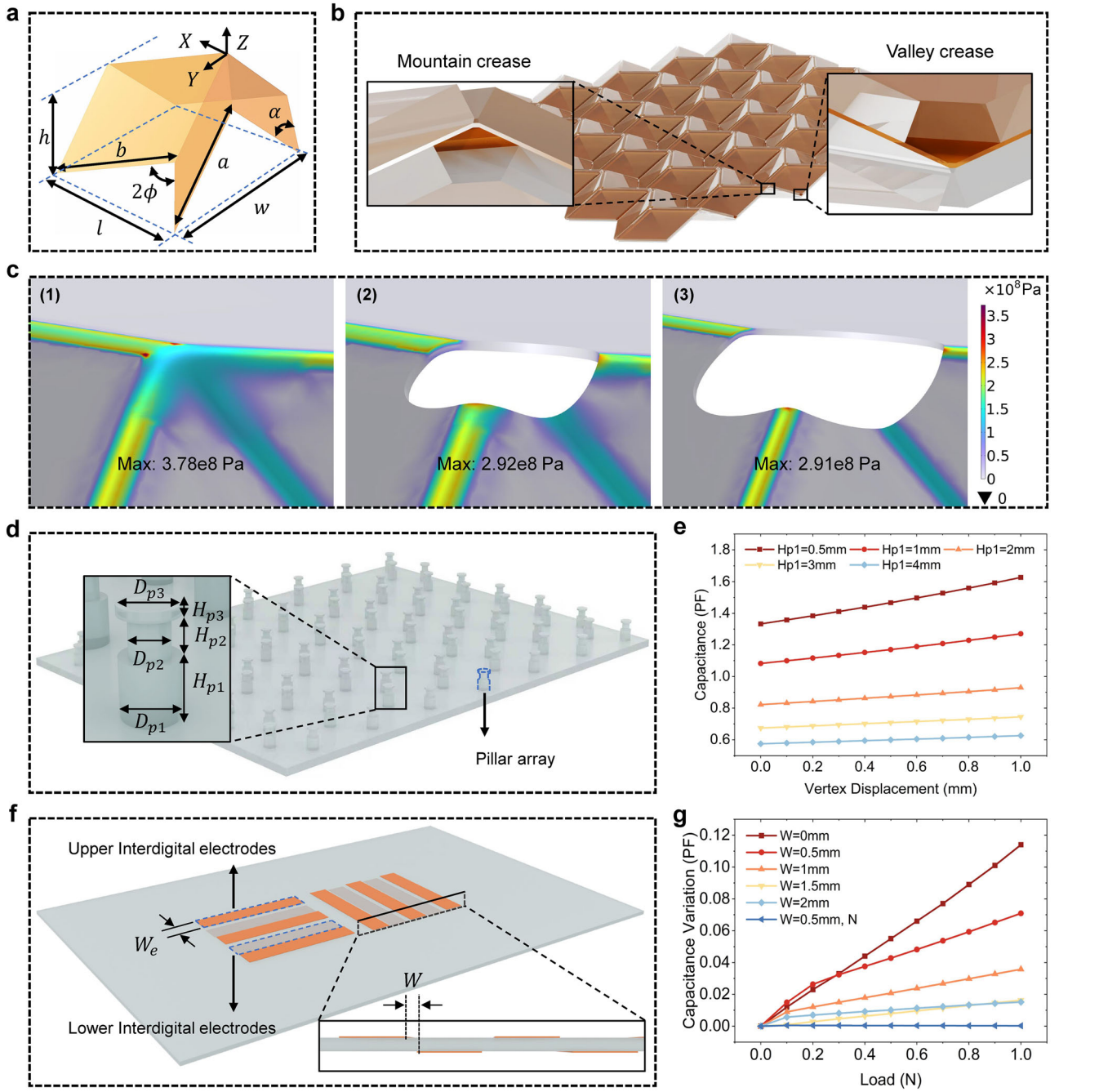

Fig. 2 | Structure design of the proposed e-skin. a Geometric definitions of Miura-ori cell. **b** Schematic of the multi-layer origami structure with crease optimizations. Different patterns were implemented for the upper and lower stiffeners. **c** Vertex cut optimizations. Stress distribution of (1) No vertex cut. (2) Circular cut with radius of 0.5 mm. (3) Circular cut with radius of 1 mm. **d** Pillar array design, each pillar was composed of three sections for a fast and convenient assembly process. **e** Capacitance variation of origami capacitor for different pillar height designs. **f** Shear-sensing layer interdigital electrodes design. **g** Capacitance variation of different interdigital electrode designs. `N' indicates the application of normal load.

The FPC layout is shown in Fig. 3b. A shielding layer was designed above the electrodes to eliminate external disturbances. An empty cell was inserted between adjacent electrodes to enhance super-resolution and expand the sensing area with fewer sensing units. The durability of the FPC under different folding scenarios is shown in Fig. S17. Additionally, the performance of this circuit was tested under various power supply conditions and grounding configurations. It was also tested across various environments, including different temperatures and humidity levels, as shown in Figs. S19 and S20, respectively. Finally, a fabricated FPC with double-layer stiffeners is shown in Fig. 3c. The detailed fabrication process is provided in Fig. S12.

Characterization and performance

Origami structures can enhance super-resolution by enabling deformation transmission. In practical applications, deformation cannot be transmitted infinitely. Therefore, the characteristics and sensing performance of the proposed e-skin were tested and evaluated. Fig. 4a shows the coordinate definition for a planar configuration (6 × 6) with 9 electrodes (S1–S9). The curved configuration follows a similar coordinate system with 4×8 cells and eight electrodes (S1–S8), as shown in Fig. S13.

The force-displacement relations for planar and curved configurations at different electrodes are presented in Fig. 4b. Specifically, the curved structure shows lower stiffness due to altered panel geometry and folding

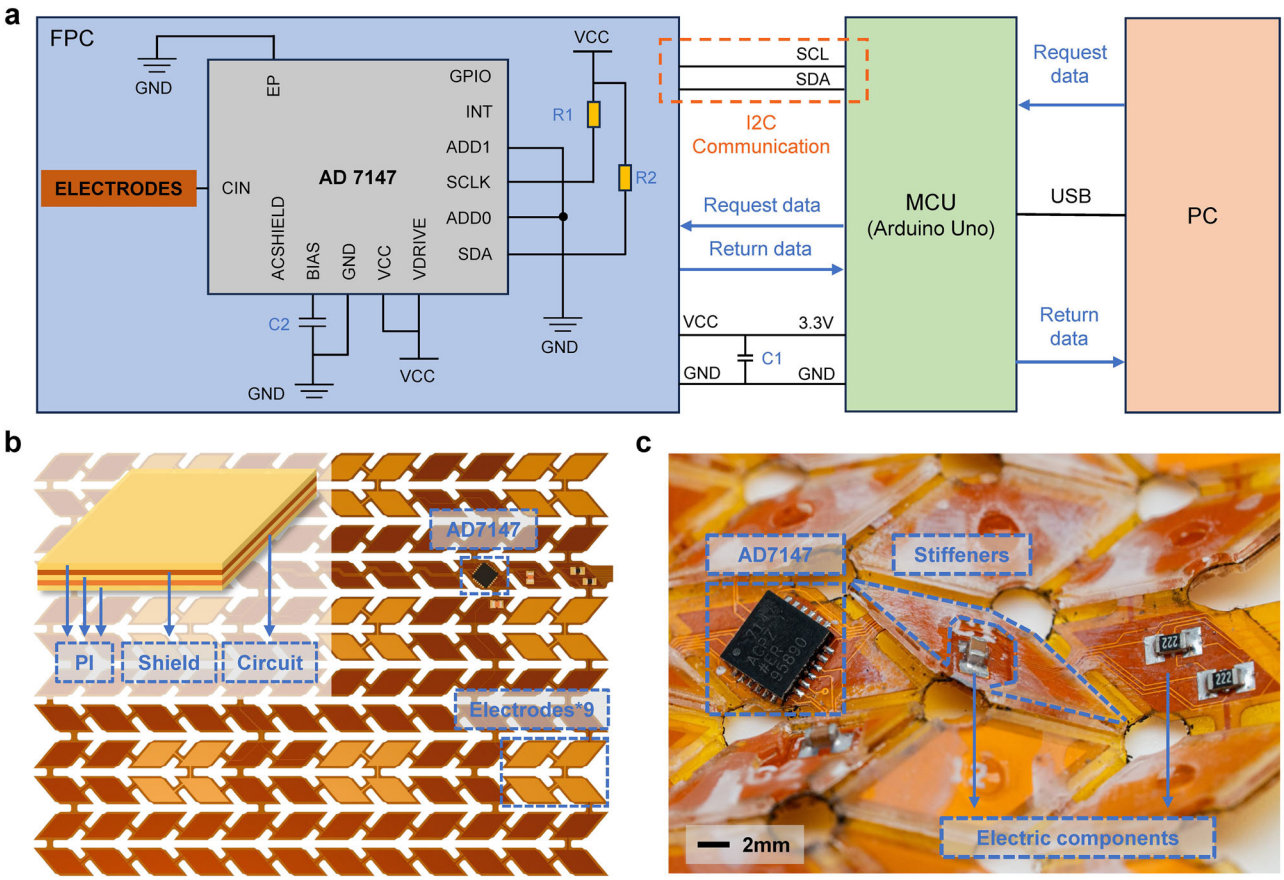

Fig. 3 | Origami-patterned circuit design. a Schematic of the designed circuit. 'CIN' port consists of 'CIN0' to 'CIN12', a total of 13 inputs. The I2C protocol was used for communication between AD7147 and the MCU (Arduino Uno), significantly reducing wiring complexity. **b** Schematic of FPC. 9 electrodes were designed for planar configuration and 8 for curved configuration. Sub-figure in the left upper corner: the FPC consists of 5 layers from top to bottom: PI (12.5 μm) with adhesive (15 μm), shield (copper, 12 μm), PI (25 μm), electrodes and circuit (copper, 12 μm), and PI (12.5 μm) with adhesive (15 μm). **c** Photo of fabricated FPC with stiffeners.

properties. Furthermore, edge cells are less stiff than central cells because they have fewer neighboring cells; this can be addressed by increasing the pillar dimensions at the edges. Finally, the slope increases with load, as deformation propagates to more cells.

Force-capacitance responses for center and edge cells are shown in Fig. 4c, d. The responses are nearly linear, regardless of the distance over which the deformation is transmitted. This is mainly due to the superposition of nonlinear stiffness (Fig. 4a) and nonlinear capacitance changes during unfolding (Fig. S10). These effects partially compensate for each other. As the deformation propagation distance increases, signal changes decrease: from about 500 CDC output changes/N at 0-cell propagation to about 100 at 1-cell and nearly 50 at 2-cell.

Repeatability was validated by applying a normal load at cell (2,1) for 10,000 cycles. Figure 4e shows no significant fluctuations between cycles, demonstrating excellent repeatability. The signals for the first ten and last ten cycles, as well as for other cells, are shown in Figs. S15 and S16.

Response and recovery times were tested with a 1 N load at cell (2,2) (Fig. 4f). The signals, measured at 100 Hz (Arduino Uno), stabilized within one period after loading. They stabilized within two periods after unloading. This yields response and recovery times of about 10 ms and 20 ms, respectively. Such performance meets most human-machine interaction needs. Faster MCUs (e.g., STM32) and optimized pillar materials with less viscoelasticity could improve response speed.

The hysteresis for center and edge cells is shown in Fig. 4g and h. The pillar array and the elastomer scalars introduce no significant hysteresis, as external loads are transmitted through the origami skeleton. Consequently, the e-skin exhibits negligible hysteresis for both central and edge cells.

Shear-sensing performances are shown in Fig. 4i. The shear force-CDC output relationships were nearly linear in both X and Y directions due to the large shear stiffness of the shear-sensing layer. Additionally, the presence of a normal load has a small effect on shear sensing; with a 1 N normal load, the outputs increased only slightly (5.61% in X and 4.71% in Y). Figure 4j shows the F-CDC output relationships for different-sized cylindrical indenters. When the indenter covers within a single cell, the origami skeleton ensures the signal is unaffected by indenter size. This is why force magnitude, not pressure, was chosen as the performance metric. If the indenter spans several cells, all compressed cells deform uniformly. Their deformation transfer characteristics remain unchanged (Fig. S18). Figure 4k shows proximity sensing for conductive plates of various sizes. Capacitance changes with plate size due to the different effective area. Proximity signals at a given distance are proportional to plate area. This allows distance estimation for conductive objects, such as measuring the distance between a hand and the e-skin. However, since this system targets human-machine interaction and uses capacitive sensing, it can detect only conductive objects.

Machine learning implementation

To enhance localization and force estimation performance, three machine learning algorithms-convolutional neural networks (CNNs), multilayer perceptrons (MLPs), and residual MLPs (ResMLPs)-were implemented and compared. For dataset collection, force-controlled indentations ranging from 0.2 N to 1 N (in 0.05 N increments) were applied across the e-skin. Load positions covered 0–87 mm (X) and 0-54 mm (Y) for the planar configuration, and 0–102 mm (X) and 0-66° (R) for the curved configuration, with 3 mm/3° spacing, yielding 9690 and 13,685 data points, respectively. The datasets were then divided into training (70%), validation (15%),

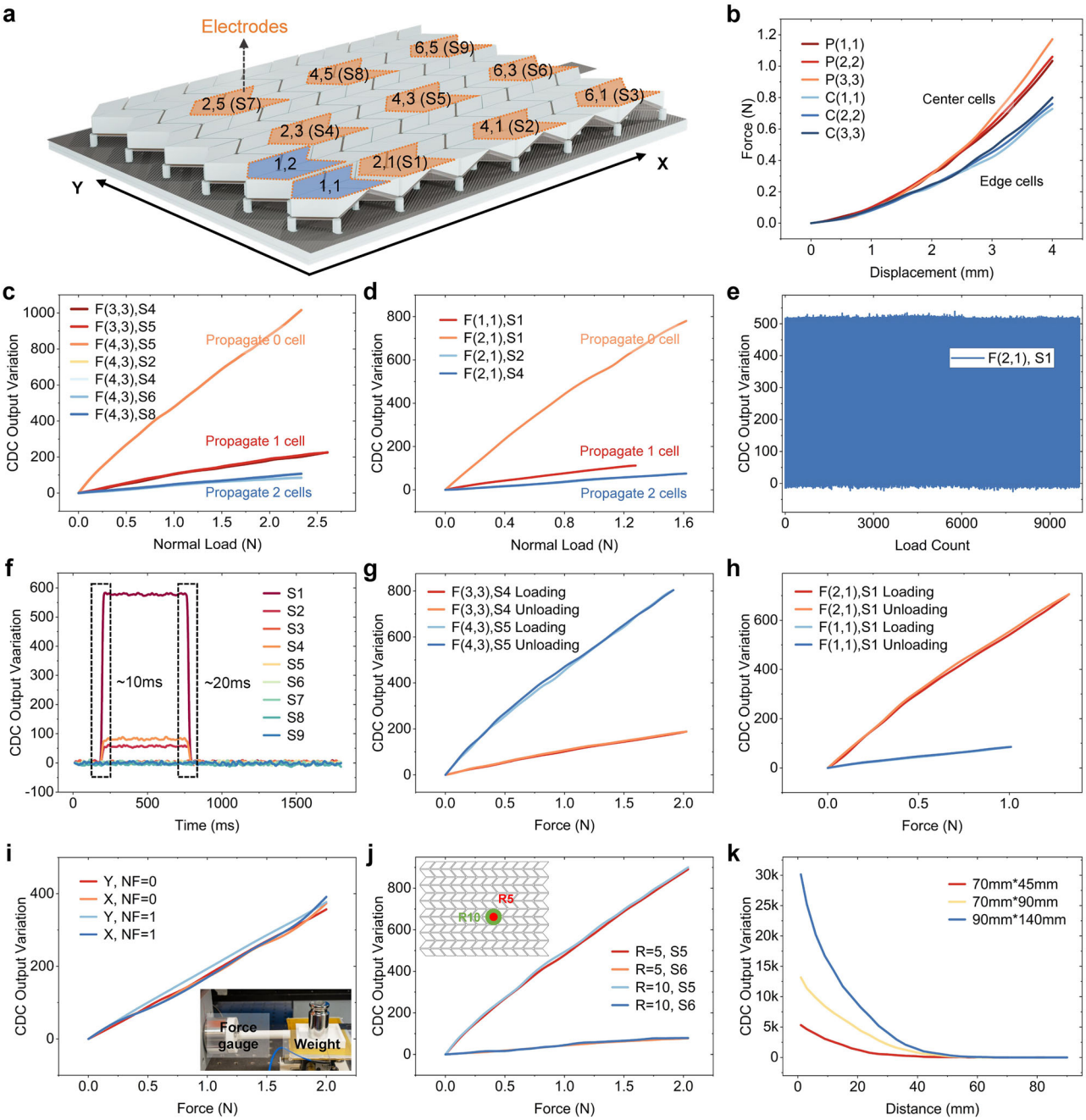

Fig. 4 | Characteristics and performances of developed e-skin. a Coordinate definition. **b** Force-displacement curves in different cells for both planar (P) and curved (C) configurations. **c** Force-CDC output variation curve for center cells. "F(3,3) S4" indicates the capacitance change of the electrode S4 when loading in cell (3,3). **d** Force-CDC output variation curve for edge cells. **e** Repeatability test results: readout from S1 when a 1 N load was applied in cell (2,1) for 10,000 times. **f** Response and recovery time when an external load of 1 N was applied at (2,1) and removed. **g** Hysteresis of center cells. **h** Hysteresis of edge cells. **i** Shear-force sensing performance. "X" and "Y" indicate the directions of the shear loads; "NF" indicates the magnitude of the normal force. **j** F-CDC output variation curve when using different sized indenters. **k** Proximity-sensing performances for different sizes of conductive plates.

and testing (15%) sets. After hyperparameter tuning, all three models achieved comparable accuracy. Specifically, for the curved configuration, CNN yielded mean estimation errors of 3.183 mm (X), 2.504 mm (Y), and 0.035 N (F); ResMLP, 3.403 mm, 2.541 mm, and 0.037 N; and MLP, 3.190 mm, 2.549 mm, and 0.034 N, as shown in Note S7 and Fig. S22. Although all three models showed similar accuracy, the MLP offered advantages. It has lower computational cost and a straightforward architecture. This suits future deployment on embedded or edge devices, such as Raspberry Pi, and simplifies network analysis and optimization. These efficiencies made MLP the preferred model for this task.

The MLP structure is shown in Fig. 5a. This architecture allows the model to effectively capture complex patterns in both planar and curved configurations. It includes 9 inputs for planar configurations and 8 for curved configurations, 5 hidden layers (each with 8, 16, 32, 16, and 32 neurons), and 3 outputs (X, Y, F). Each hidden layer uses the ReLU activation function, and the final layer uses the Sigmoid function to normalize outputs between 0 and 1. All input and output data were normalized before training. Figure 5b-d show the performance of the trained MLP, highlighting its high accuracy in localization and force estimation. Most localization errors were below 5 mm in both directions, and most force estimation

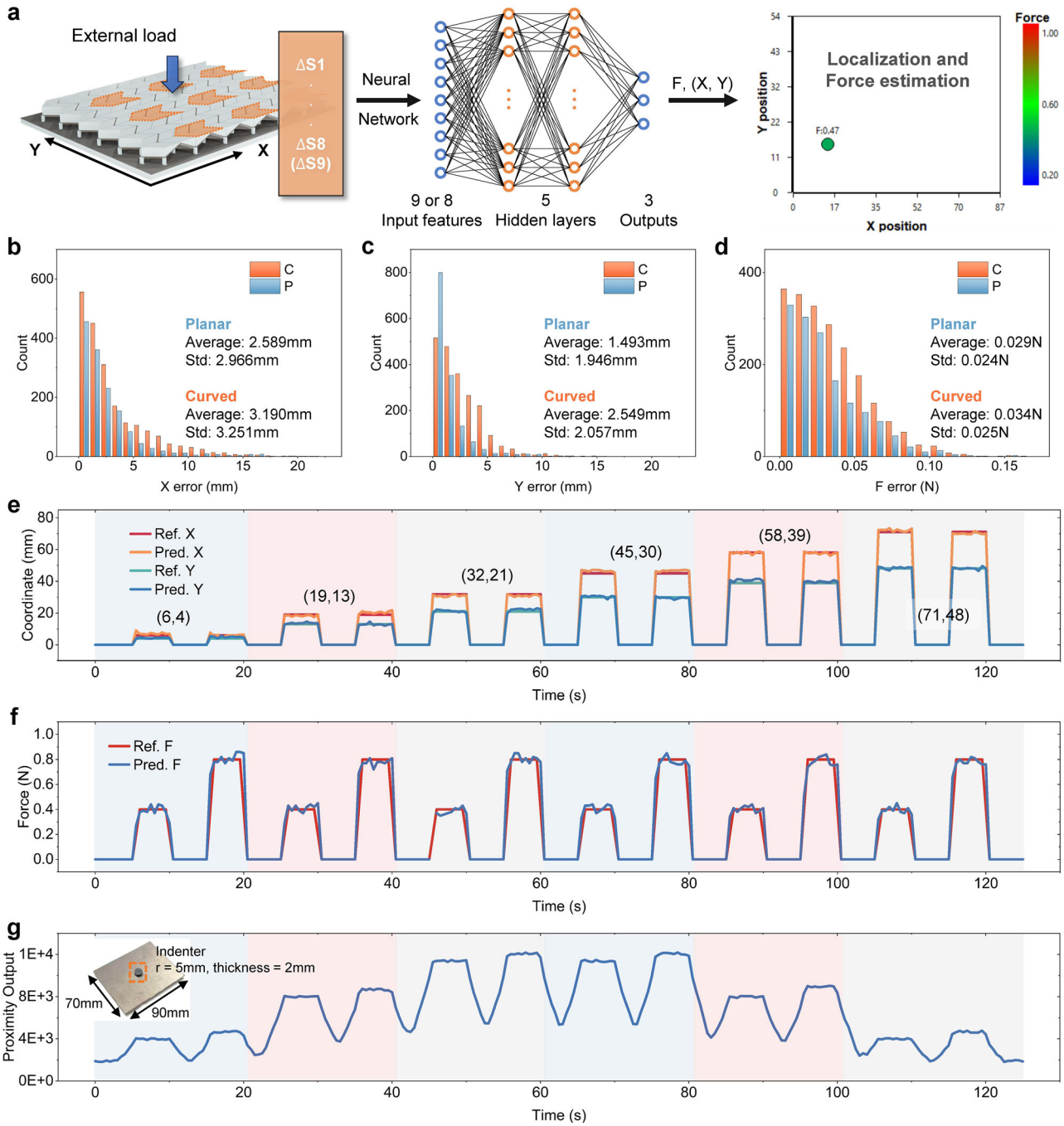

Fig. 5 | Machine learning implementation. a Schematic of machine learning workflow. **b** Localization performance in the X direction for both planar (P) and curved (C) configurations. **c** Counterpart of (**b**) in the Y direction. **d** Normal load magnitude estimation performance for both planar and curved configurations. **e**–**g** Real-time localization, force magnitude estimation, and proximity-sensing results when both tactile sensing and proximity sensing are enabled. Here, 6 locations along the diagonal of the e-skin were selected, and each was tested by applying two different forces. The indenter schematic shown in (**g**) consists of a rectangular conductive plate and a cylindrical indenter with a 2 mm-thick center.

errors were under 0.1 N. This demonstrates the model's capability to provide reliable results for both localization and normal force estimation.

Real-time localization, force estimation, and proximity-sensing results are in Fig. 5e–g. When both tactile and proximity sensing are enabled, the mutual interference is negligible because each uses different readout channels, and the FPC's shielding layer helps mitigate interference. During real-time tests, a CDC output threshold of 30 was set for tactile sensing. The model activates only when at least one of the tactile sensing signals (S1–S9) exceeds 30, eliminating influence from external noise (results without a threshold are shown in Fig. S23). Results show that localization is accurate across positions. Force estimation is slightly less stable, but its maximum error is within 0.1 N. Accuracy can be improved by expanding the training force range (now 0.2 N to 1 N in 0.05 N intervals).

To further validate performance, three additional curved samples were made using the same process. The trained MLP's generalization was shown by direct deployment—no retraining—on 210 random indentations per sample (Fig. S25). Performance stayed nearly the same, confirming strong repeatability and suitability for scalable fabrication and deployment without re-optimization. To assess the effects of sensing cell density, models were retrained with fewer electrode inputs (e.g., S1, S3, S7, S9). Results are shown

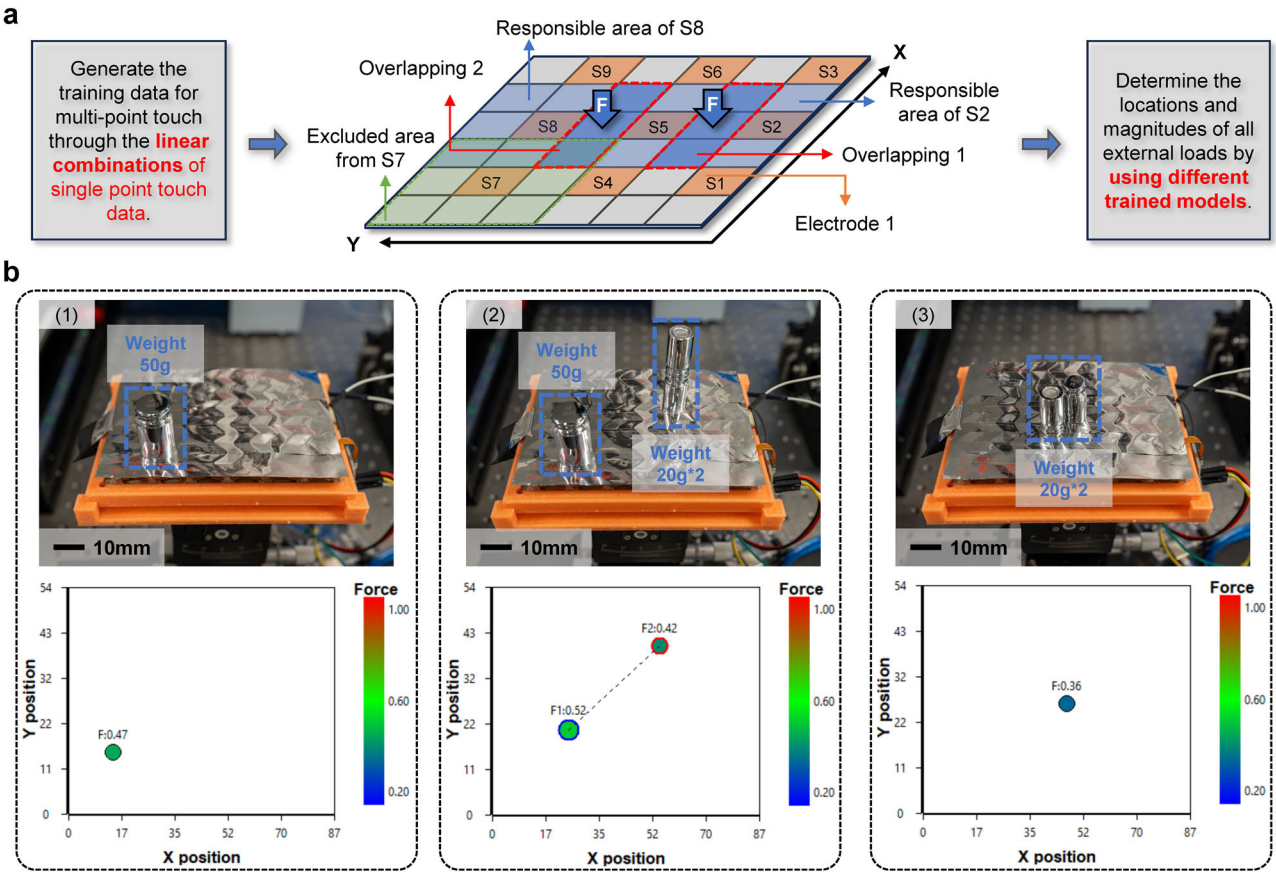

Fig. 6 | Multi-point touch realization and demonstrations. a Schematic of Multi-point touch for non-adjacent loads. The number of external loads is determined by analyzing signal changes through electrodes, and their positions and magnitudes are estimated using corresponding machine learning models. **b** Demonstration of multi-point touch for non-adjacent loads. (1) Single point touch. (2) Two external loads acting simultaneously at a large distance from each other. (3) Two adjacent external loads acting simultaneously.

in Fig. S24. Accuracy declined slightly but stayed within acceptable limits. Using only four electrodes, the SR factor can exceed 500. This means the same number of electrodes can cover a larger sensing area with little loss in accuracy.

Multi-point touch for non-adjacent loads

Most existing e-skins achieve multi-point touch using dense grids of touch sensors. This results in complex circuitry and wiring. In contrast, most super-resolution e-skins use algorithms to estimate touch position[24,26,28,34], but neither approach inherently determines the number of external loads, since models like MLPs have fixed input and output sizes. Data collection also presents major challenges, particularly due to scalability constraints and limitations in experimental design. For n-point touch, the required dataset size grows as N^n, where N is the number of single-point data points. For example, in a curved e-skin, single-point training needs 13,680 data groups. Two-point touch would require 93,571,200 ($13{,}680^2/2$) samples, which is not feasible. Data collection is also complex because a dual-load experimental setup is needed.

To overcome these challenges, we integrated origami-based analytical modeling with machine learning to realize multi-point touch for non-adjacent loads. Since the force-CDC output relationship is approximately linear (Fig. 4c and d), we generated multi-point training datasets by linearly superimposing single-point data (Fig. S28; verification shown in Fig. S29 and Table S1). Then, by monitoring the changes in readouts across each electrode and counting the number of electrodes whose readouts exceed the threshold (Note S8, Figs. S26 and S27), the number of external loads can be determined. Then, the locations and magnitudes of all external loads can be calculated by implementing the corresponding trained model.

12The workflow of the proposed method is illustrated in Fig. 6a, while demonstrations are shown in Fig. 6b. With one load, a three-output model estimates its position and magnitude (Fig. 6b(1)). With two loads at distant locations, they are separated (Fig. 6b(2)). If two adjacent loads are applied together (Fig. 6b(3)), they appear as one equivalent load. This limits our multi-point touch technique, but the equivalence is acceptable in most practical human-machine interactions. Thus, our approach is broadly applicable. A demonstration video is provided in Movie S1, and detailed performance tests are shown in Figure S30.

Demonstrations of human-machine interactions

After training the machine learning model, four curved e-skins were fabricated and mounted on a robotic arm for human-machine interactions (Fig. 7a). When touched, the e-skin's origami structure deforms, changing the capacitance in the embedded electrodes. The AD7147 captures these variations. A TCA 9548A I2C switch and Arduino Uno board process the data and transmit it to a PC. The PC performs localization, force estimation, and proximity analysis. Based on these results, corresponding control signals are sent back to the robotic arm. Fig. 7b, c shows tactile sensing-based control under normal and shear loads. Applying a normal force (perpendicular push or pressure) in different directions moves the robotic arm in the same direction (Fig. 7b). Shear forces (sideways pushes) also control movement; shear applied clockwise or counterclockwise rotates the joints accordingly (Fig. 7c).

Beyond tactile sensing-based control, proximity sensing expands interaction possibilities (Fig. 8). In translational control (Fig. 8a), the robotic arm moves in response to a nearby hand and maintains the distance within a target range. This allows the robotic arm to follow

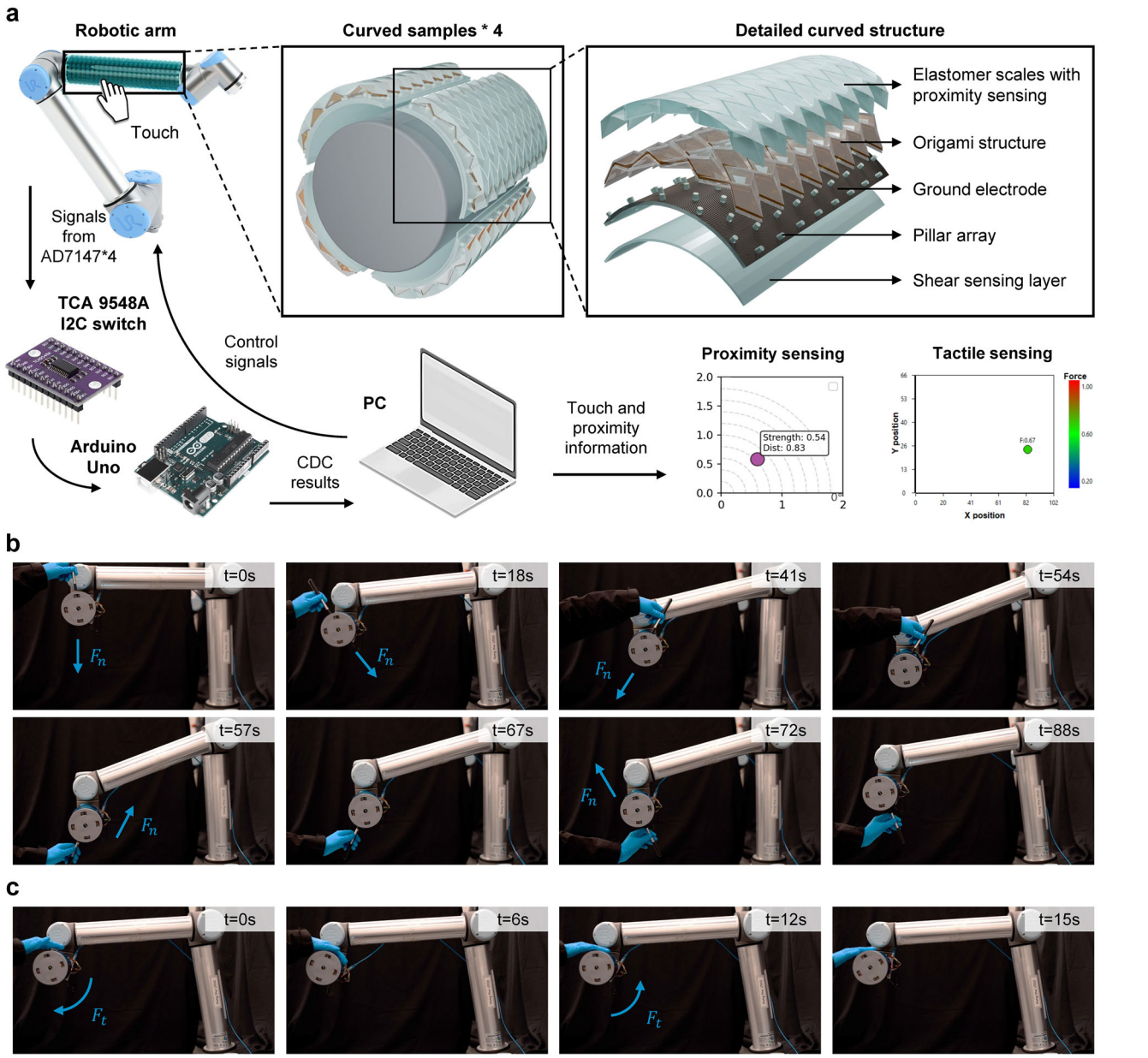

Fig. 7 | Demonstrations of tactile sensing-based human-machine interactions. **a** Schematic of e-skin mounting, signal transmission, and control of the robotic arm. Four curved e-skins were utilized. They are all connected to a TCA9548A I2C switch for I2C communications. **b** Normal-load-based robotic arm translational control. When external forces are applied along different directions, the robotic arm will move correspondingly. **c** Shear-load-based robotic arm rotational control. When shear forces are applied along different directions (clockwise or counterclockwise), the corresponding joints will rotate in the respective directions.

human motion. For safety applications (Fig. 8b), the arm decelerates and stops when the proximity signal reaches a threshold, preventing collisions. Furthermore, with proximity sensing in four directions, the robotic arm achieves autonomous conductive obstacle avoidance (Fig. 8c). As it approaches an "L"-shaped conductive obstacle, the arm dynamically adjusts its path to avoid collisions. This capability enables the robotic arm to replan its trajectory and continue moving without interrupting the task when it encounters a human during operation. Together, tactile and proximity sensing give the robotic arm environmental awareness, supporting intuitive human-machine interactions. A demonstration video is available in Movie S1.

Discussion

Inspired by fish skin, we developed an origami-enabled super-resolution capacitive e-skin. The origami architecture enhances super-resolution by transmitting deformation between cells. A multilayer design enables the separation of normal load, shear load, and proximity sensing for conductive objects. To ensure adaptability, we also designed and fabricated curved e-skins that can conform to curved surfaces. Building on these structural advancements, we incorporated machine learning algorithms to achieve accurate localization and force estimation. Furthermore, the combination of theoretical analysis with machine learning enabled multi-touch for non-adjacent loads. The cumbersome multi-point data acquisition process was simplified by generating multi-touch data through linear combinations of single-touch datasets, broadening the potential for complex human-machine interactions. To validate the developed e-skin, four modular curved e-skins were mounted on a robotic arm for demonstrations involving both tactile and proximity-based human-machine interactions. These results demonstrate the system's ability to facilitate intuitive human-machine interactions, laying the groundwork for embodied intelligence.

However, limitations persist. the capacitive proximity-sensing layer effectively detects conductive objects such as human skin or metal obstacles,

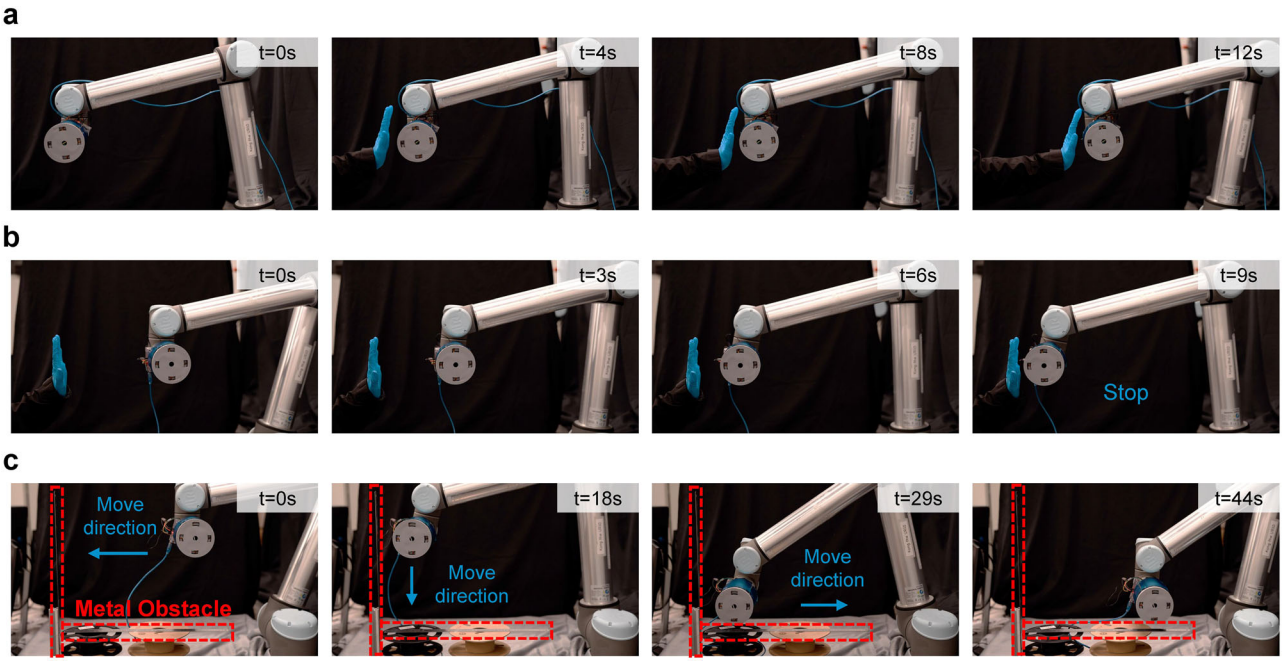

Fig. 8 | Proximity sensing-based human-machine interactions. a Contact-free robotic arm translation control. **b** Proximity detection-based collision protection. When the robotic arm approaches a human hand to a certain distance, it will automatically stop. **c** Automatic conductive obstacle (a 'L' shape metal obstacle) avoidance for the robotic arm based on proximity detection, simulating scenarios where a robotic arm encounters a human during operation. Note: In real applications, non-conductive obstacles are not detected by the proximity-sensing layer. As a safety-by-design measure, the system should be complemented with traditional safety measures (e.g., physical bumpers, area scanners) in environments with mixed-material obstacles.

it cannot detect non-conductive materials (e.g., plastics, wood, fabrics). This limitation is inherent to electric field-based capacitive sensing. In the context of human-machine interaction-the primary application envisioned—this limitation is mitigated by the fact that humans are conductive, and many industrial environments contain conductive structures. However, for broader deployment in unstructured environments and multi-material workspaces, this constraint must be considered. To extend proximity detection to non-conductive objects, several engineering approaches could be integrated, for example, the integration of ultrasonic or infrared sensors inside the origami-shaped circuit.

Methods

Material selection

The origami stiffeners were fabricated from 0.5 mm-thick poly(methyl methacrylate) plates. The middle layer was constructed by a multi-layer FPC, from top to bottom: PI (12.5 μm) with adhesive (15 μm), a shield layer (copper, 1/3 oz, around 12 μm thickness), a PI substrate (25 μm), a circuit layer (copper, 1/3 oz, around 12 μm), and the bottom PI (12.5 μm) with adhesive (15 μm), resulting in a total thickness of about 104 μm. Ecoflex 00-30 (Smooth-On Inc.) was used for both the upper elastomer scales and the pillar array to provide structural softness. The shear-force sensing layer consists of Ecoflex 00-30 with copper electrodes. The proximity-sensing layer consists of a 25 μm-thick single-sided aluminized PI film.

Fabrication process

During fabrication, the FPC was produced, and the electronic components were assembled. Then, the FPC was bonded to a 25 μm-thick PI film using double-sided adhesives for easy fabrication (due to the relatively thick FPC, direct folding would result in high folding stiffness, reducing sensitivity). Therefore, during FPC design, only the essential circuit connection areas are retained in the fold zone, while the rest are removed (Fig. 3b). The upper and lower stiffeners were laser-cut into the designed pattern and then bonded to the FPC by adhesive to form the multi-layer origami structure. Molds were used during the bonding process to align different layers. The pillar arrays, top elastomer scales, and bottom shear-sensing layer were molded. Due to the multi-section design of the pillars, the origami structure can be conveniently assembled with the pillar array in the bottom vertices. Then, the elastomer scales were bonded to the upper panels using Silpoxy (Smooth-on Inc., USA), along with the proximity-sensing layer. Finally, the shear-sensing layer was directly adhered to the remaining components, then to the robotic arm or other destinations. The schematic of the fabrication process is shown in Fig. S12.

Sensor characterization

The force-displacement curve was measured using a compression testing machine (Instron 68SC-05), while the force-CDC output curve and hysteresis were also tested on the same platform. The repeatability and response/recovery times were tested on a moving platform equipped with a force gage (SIMBATOUCH SBT673) (Fig. S14). The machine learning training data were collected using a four-axis mobile platform with three-axis translation and one rotation, as shown in Fig. S14. This mobile platform is controlled via LabVIEW automation programs and automatically collects training data for machine learning. The sampling intervals for machine learning data were: 1) Planar case: 3 mm sampling intervals were used in both the X and Y directions, resulting in a total of 513 locations (27 × 19) for each magnitude of normal load (Overall used area: 78 mm by 54 mm). 2) Curved Surface Case: The Y interval was maintained at 3 mm, while the circumferential interval was set at 3°, corresponding to an arc length of ~3 mm (resulting in a total of 588 locations). For the normal load magnitude, values ranging from 0.2 N to 1.0 N, with increments of 0.05 N, were applied via a linear bearing with a specific weight. To ensure that the e-skin reached a stable state before signal collection, a 2-second delay was implemented after the external load was applied.

Regarding the performance of sensors under varying temperature and humidity conditions, humidity was controlled by placing the sensors in a semi-enclosed chamber (open at the top to apply force) equipped with a humidifier (laboratory-standard humidity is ~50%). Temperature variations were achieved by exposing the sensors to heating lamps. For testing

under different power supply and grounding conditions, the external power supply selected is the MCH-K302D (MCH Instruments CO., Ltd.), and the waveform was measured with an oscilloscope (Tektronix MDO34, TEKTRONIX, INC.). All numerical simulations were performed using COMSOL Multiphysics.

Demonstration setup

The curved origami e-skin assembly was installed on the UR10 robotic arm (Universal Robots) tool flange for testing. Data acquisition, model inference, and robotic arm control were all handled by a laptop. E-skin signals were transmitted to a TCA 9548A I2C switch, then to an Arduino Uno, and finally to the laptop via USB, enabling localization and force estimation. These results, along with proximity sensing data, were displayed in the interface. All machine learning and visualization code ran in Visual Studio Code (Python 3.11). Based on the detected load location and magnitude, corresponding control signals were generated and sent to the robotic arm through Visual Studio Code.

Data availability

The authors declare that all data needed to evaluate the conclusions are available in the article and the Supplementary Information. All data are available from the corresponding authors upon request. All code and data used for machine learning in this work are available in https://github.com/XuqianUST/Multimodal-E-skin.

Received: 17 November 2025; Accepted: 4 March 2026;
Published online: 25 March 2026

References

1. Wang, X., Gu, Y., Xiong, Z., Cui, Z. & Zhang, T. Silk-molded flexible, ultrasensitive, and highly stable electronic skin for monitoring human physiological signals. *Adv. Mater.* **26**, 1336–1342 (2014).
2. Park, J. et al. Giant tunneling piezoresistance of composite elastomers with interlocked microdome arrays for ultrasensitive and multimodal electronic skins. *ACS Nano* **8**, 4689–4697 (2014).
3. Jian, M. et al. Flexible and highly sensitive pressure sensors based on bionic hierarchical structures. *Adv. Funct. Mater.* **27**, 1606066 (2017).
4. Chen, W. et al. Structural engineering for high sensitivity, ultrathin pressure sensors based on wrinkled graphene and anodic aluminum oxide membrane. *ACS Appl. Mater. Interfaces* **9**, 24111–24117 (2017).
5. Takei, K. et al. Nanowire active-matrix circuitry for low-voltage macroscale artificial skin. *Nat. Mater.* **9**, 821–826 (2010).
6. Mannsfeld, S. C. et al. Highly sensitive flexible pressure sensors with microstructured rubber dielectric layers. *Nat. Mater.* **9**, 859–864 (2010).
7. Luo, Y. et al. Flexible capacitive pressure sensor enhanced by tilted micropillar arrays. *ACS Appl. Mater. Interfaces* **11**, 17796–17803 (2019).
8. Zang, Y. et al. Flexible suspended gate organic thin-film transistors for ultra-sensitive pressure detection. *Nat. Commun.* **6**, 6269 (2015).
9. Shin, S.-H. et al. Integrated arrays of air-dielectric graphene transistors as transparent active-matrix pressure sensors for wide pressure ranges. *Nat. Commun.* **8**, 14950 (2017).
10. Chen, Z. et al. Flexible piezoelectric-induced pressure sensors for static measurements based on nanowires/graphene heterostructures. *ACS Nano* **11**, 4507–4513 (2017).
11. Wang, X. et al. Dynamic pressure mapping of personalized handwriting by a flexible sensor matrix based on the mechanoluminescence process. *Adv. Mater.* **27**, 2324–2331 (2015).
12. Wang, Z. L., Chen, J. & Lin, L. Progress in triboelectric nanogenerators as a new energy technology and self-powered sensors. *Energy Environ. Sci.* **8**, 2250–2282 (2015).
13. Li, Y. et al. Visualization and standardized quantification of surface charge density for triboelectric materials. *Nat. Commun.* **15**, 6004 (2024).
14. Hu, J., Cao, D., Li, Y. & Liu, H. Polymer-based optical waveguide tactile sensing method for 3-D surfaces. *IEEE Sens. J.* **23**, 8761–8768 (2023).
15. Chen, S. et al. Flexible wearable sensors for cardiovascular health monitoring. *Adv. Healthc. Mater.* **10**, 2100116 (2021).
16. Tomo, T. P. et al. A new silicone structure for uskin—a soft, distributed, digital 3-axis skin sensor and its integration on the humanoid robot icub. *IEEE Robot. Autom. Lett.* **3**, 2584–2591 (2018).
17. Dai, H. et al. Split-type magnetic soft tactile sensor with three-dimensional force decoupling. *Adv. Mater.* 2310145 (2023).
18. Man, J., Zhang, J., Chen, G., Xue, N. & Chen, J. A tactile and airflow motion sensor based on flexible double-layer magnetic cilia. *Microsyst. Nanoeng.* **9**, 12 (2023).
19. Chorsi, M. T. et al. Piezoelectric biomaterials for sensors and actuators. *Adv. Mater.* **31**, 1802084 (2019).
20. Lin, Z. et al. Insights into materials, physics, and applications in flexible and wearable acoustic sensing technology. *Adv. Mater.* **36**, 2306880 (2024).
21. Someya, T. et al. A large-area, flexible pressure sensor matrix with organic field-effect transistors for artificial skin applications. *Proc. Natl. Acad. Sci. USA* **101**, 9966–9970 (2004).
22. Nguyen, T. T.-H. et al. Field effect transistor based wearable biosensors for healthcare monitoring. *J. Nanobiotechnol.* **21**, 411 (2023).
23. Park, K. et al. A biomimetic elastomeric robot skin using electrical impedance and acoustic tomography for tactile sensing. *Sci. Robot.* **7**, eabm7187 (2022).
24. Yan, Y. et al. Soft magnetic skin for super-resolution tactile sensing with force self-decoupling. *Sci. Robot.* **6**, eabc8801 (2021).
25. Guo, J. et al. Flexible plasmonic optical tactile sensor for health monitoring and artificial haptic perception. *Adv. Mater. Technol.* **8**, 2201506 (2023).
26. Sun, H. & Martius, G. Guiding the design of superresolution tactile skins with taxel value isolines theory. *Sci. Robot.* **7**, eabm0608 (2022).
27. Li, Y. et al. A machine learning-assisted multifunctional tactile sensor for smart prosthetics. *InfoMat* **5**, e12463 (2023).
28. Hu, H. et al. Wireless flexible magnetic tactile sensor with super-resolution in large-areas. *ACS Nano* **16**, 19271–19280 (2022).
29. Jasim, B. & Taheri, P. An origami-based portable solar panel system. In *2018 IEEE 9th Annual Information Technology, Electronics and Mobile Communication Conference (IEMCON)*, 199–203 (IEEE, 2018).
30. Hong, S. et al. Nature-inspired, 3d origami solar steam generator toward near full utilization of solar energy. *ACS Appl. Mater. Interfaces* **10**, 28517–28524 (2018).
31. Liu, S., Lu, G., Chen, Y. & Leong, Y. W. Deformation of the Miura-Ori patterned sheet. *Int. J. Mech. Sci.* **99**, 130–142 (2015).
32. Tachi, T. Generalization of rigid-foldable quadrilateral-mesh origami. *J. Int. Assoc. Shell Spat. Struct.* **50**, 173–179 (2009).
33. Deng, Y. et al. Curved display based on programming origami tessellations. *Microsyst. Nanoeng.* **7**, 101 (2021).
34. Li, T. et al. An artificial intelligence-motivated skin-like optical fiber tactile sensor. *Adv. Intell. Syst.* **5**, 2200460 (2023).
35. Hu, H. et al. Large-area magnetic skin for multi-point and multi-scale tactile sensing with super-resolution. *npj Flex. Electron.* **8**, 42 (2024).
36. Leong, C. Y., Cheng, X., Cui, J., Gunawardena, D. S. & Tam, H.-Y. Artificial skin based on polymer optical fiber Bragg grating arrays for robotic tactile perception. *J. Lightwave Technol.* **42**, 3022–3029 (2023).
37. Lu, Z. et al. A low-cost super-resolution tactile sensor: design, fabrication and validation. *IEEE Sens. J.* (2024).
38. Pereira Resende da Costa, A. C., Filosa, M., Barbosa Soares, A. & Oddo, C. M. Type II mechanoreceptors and cuneate spiking neuronal network enable touch localization on a large-area e-skin. *Nat. Mach. Intell.* **7**, 1278–1291 (2025).

39. Sohn, K.-S. et al. An extremely simple macroscale electronic skin realized by deep machine learning. *Sci. Rep.* **7**, 11061 (2017).
40. Chen, X. et al. Full-textile less-wires large-area flexible robot electronic skin for human–robot interaction. *IEEE Sens. J.* **26**, 1705–1715 (2025).
41. Shao, B. et al. Large-area, untethered, metamorphic, and omnidirectionally stretchable multiplexing self-powered triboelectric skins. *Nat. Commun.* **15**, 1238 (2024).
42. Berman, A. et al. A skin-inspired, capacitive array for tactile modulus detection via a scalable rigid-island architecture. *npj Flexible Electron.* (2025).

Acknowledgements

This study was funded by the Research Grants Council of Hong Kong under the General Research Fund (16204124), and the Innovation and Technology Commission (project: GHP/021/22) of HKSAR.Q.X.'s visit to Southern University of Science and Technology was supported by the SUSTech Fellow program.All the funders played no role in the study design, data collection, analysis and interpretation of data, or the writing of this manuscript.

Author contributions

H.Y., W.H. and S.Y. conceived and supervised the project. Q.X. designed, fabricated, and tested the E-skins. Q.X. and Z.Y. carried out the theoretical analysis and FEA; Build the data collection platform. Q.X., B.Z. and Y.C. developed machine learning algorithms and trained the model. Q.X. and B.Z. conduct the demonstrations. R.J. and Y.C. helped with article writing. All authors contributed to the discussion of the results.

Competing interests

The authors declare no competing interests.

Additional information

Supplementary information The online version contains supplementary material available at https://doi.org/10.1038/s41528-026-00563-3.

Correspondence and requests for materials should be addressed to Wei Hong or Hongyu Yu.